9292 *Biochemistry* **2010,** *49,* 9292–9305
DOI: 10.1021/bi101226n

BIOCHEMISTRY
including biophysical chemistry & molecular biology
*Article*

# Biochemical and Structural Characterization of Bisubstrate Inhibitors of BasE, the Self-Standing Nonribosomal Peptide Synthetase Adenylate-Forming Enzyme of Acinetobactin Synthesis[†,‡]

Eric J. Drake,[§] Benjamin P. Duckworth,[∥] João Neres,[∥] Courtney C. Aldrich,[∥] and Andrew M. Gulick*[,§]

[§]*Hauptman-Woodward Institute and Department of Structural Biology, University at Buffalo, Buffalo, New York 14203-1102, United States, and* [∥]*Center for Drug Design, University of Minnesota, Minneapolis, Minnesota 55455, United States*

*Received August 2, 2010; Revised Manuscript Received September 17, 2010*

ABSTRACT: The human pathogen *Acinetobacter baumannii* produces a siderophore called acinetobactin that is derived from one molecule each of threonine, histidine, and 2,3-dihydroxybenzoic acid (DHB). The activity of several nonribosomal peptide synthetase (NRPS) enzymes is used to combine the building blocks into the final molecule. The acinetobactin synthesis pathway initiates with a self-standing adenylation enzyme, BasE, that activates the DHB molecule and covalently transfers it to the pantetheine cofactor of an aryl-carrier protein of BasF, a strategy that is shared with many siderophore-producing NRPS clusters. In this reaction, DHB reacts with ATP to form the aryl adenylate and pyrophosphate. In a second partial reaction, the DHB is transferred to the carrier protein. Inhibitors of BasE and related enzymes have been identified that prevent growth of bacteria on iron-limiting media. Recently, a new inhibitor of BasE has been identified via high-throughput screening using a fluorescence polarization displacement assay. We present here biochemical and structural studies to examine the binding mode of this inhibitor. The kinetics of the wild-type BasE enzyme is shown, and inhibition studies demonstrate that the new compound exhibits competitive inhibition against both ATP and 2,3-dihydroxybenzoate. Structural examination of BasE bound to this inhibitor illustrates a novel binding mode in which the phenyl moiety partially fills the enzyme pantetheine binding tunnel. Structures of rationally designed bisubstrate inhibitors are also presented.

Through the rapid spread of resistance mechanisms, microbial pathogens continue to challenge our efforts to develop new antibiotics. Increasingly, both community and hospital acquired strains of bacteria are being identified that are resistant to many, and sometimes all, known classes of antibiotics. This development warrants an effort to identify compounds that target novel bacterial pathways as a possible mechanism to develop new antibiotics. Bacterial pathways that are responsible for the production or acquisition of essential nutrients have been identified as an attractive and previously unexploited target for inhibition (*1*, *2*).

Despite the abundance of iron in the environment, the toxicity and low solubility of iron(III) pose a challenge to bacteria, nearly all strains of which require micromolar concentrations of iron for growth (*3*). Bacteria have therefore evolved synthetic pathways for the production of a diverse array of siderophores, molecules with remarkably high affinities (*4*) for iron. These compounds are secreted, bind to iron, and are subsequently taken into the cells through specialized transporters (*3*). Once taken into the cell, the cellular environment (*5*) or catalytic processes (*6*) trigger the release of iron, allowing it to be incorporated into a wide variety of proteins where it plays essential structural or catalytic roles.

Many bacteria use a family of modular enzymes called nonribosomal peptide synthetases (NRPSs)[1] to synthesize peptide siderophores. The NRPS enzymes have been compared to molecular assembly lines as the proteins are organized with multiple catalytic domains that can be joined in a single, modular megasynthetase (*7*, *8*). In these enzymes, the nascent peptide is attached to the phosphopantetheine cofactor of a peptidyl carrier

[†]This work is supported in part by NIH Grant GM-068440 (to A.M. G.) and AI-070219 (to C.C.A). Diffraction data were collected at the Cornell High Energy Synchrotron Source which is supported by the National Science Foundation under Award DMR 0225180 and the National Institutes of Health through its National Center for Research Resources under Award 5 P41 RR001646-23 and at the Stanford Synchrotron Radiation Lightsource, a national user facility operated by Stanford University on behalf of the U.S. Department of Energy, Office of Basic Energy Sciences. The SSRL Structural Molecular Biology Program is supported by the Department of Energy, Office of Biological and Environmental Research, and by the National Institutes of Health, National Center for Research Resources, Biomedical Technology Program, and the National Institute of General Medical Sciences.

[‡]The structure factors and coordinates of the BasE protein bound to **5** (3O82), **7** (3O83), and **8** (3O84) have been deposited with the Protein Data Bank.

*To whom correspondence should be addressed. Phone: (716) 898-8619. Fax: (716) 898-8660. E-mail: gulick@hwi.buffalo.edu.

[1]Abbreviations: ANL superfamily, family of adenylate-forming enzymes composed of the acyl-CoA synthetases, NRPS adenylation domains, and firefly luciferases; ArCP, aryl carrier protein; BA, benzoic acid; BTP, 1,3-bis{[tris(hydroxymethyl)methyl]amino}propane; CBAL, 4-chlorobenzoyl-CoA ligase; CoA, coenzyme A; DHB, 2,3-dihydroxybenzoic acid; DHB-AMS, 5′-*O*-[*N*-(2,3-dihydroxylbenzoyl)sulfamoyl]-adenosine; Fl-Sal-AMS, 2′-*O*-{2-[2-(2-{[(fluorescein-5-yl)carbonyl]-amino}ethoxy)ethoxy]ethoxy}-5′-*O*-[*N*-(2-hydroxybenzoyl)sulfamoyl]-adenosine triethylammonium salt; 3-HBA, 3-hydroxybenzoic acid; HTS, high-throughput screening; IMAC, immobilized metal ion affinity chromatography; MesG, 7-methyl-6-thioguanosine; MPD, 2-methyl-pentane-2,4-diol; NRPS, nonribosomal peptide synthetase; PCP, peptidyl carrier protein; rms, root mean square; PK, pharmacokinetic; Sal, salicylic acid; Sal-AMS, 5′-*O*-[*N*-(salicyl)sulfamoyl]adenosine; TEV, tobacco etch virus.

 Published on Web 09/20/2010 

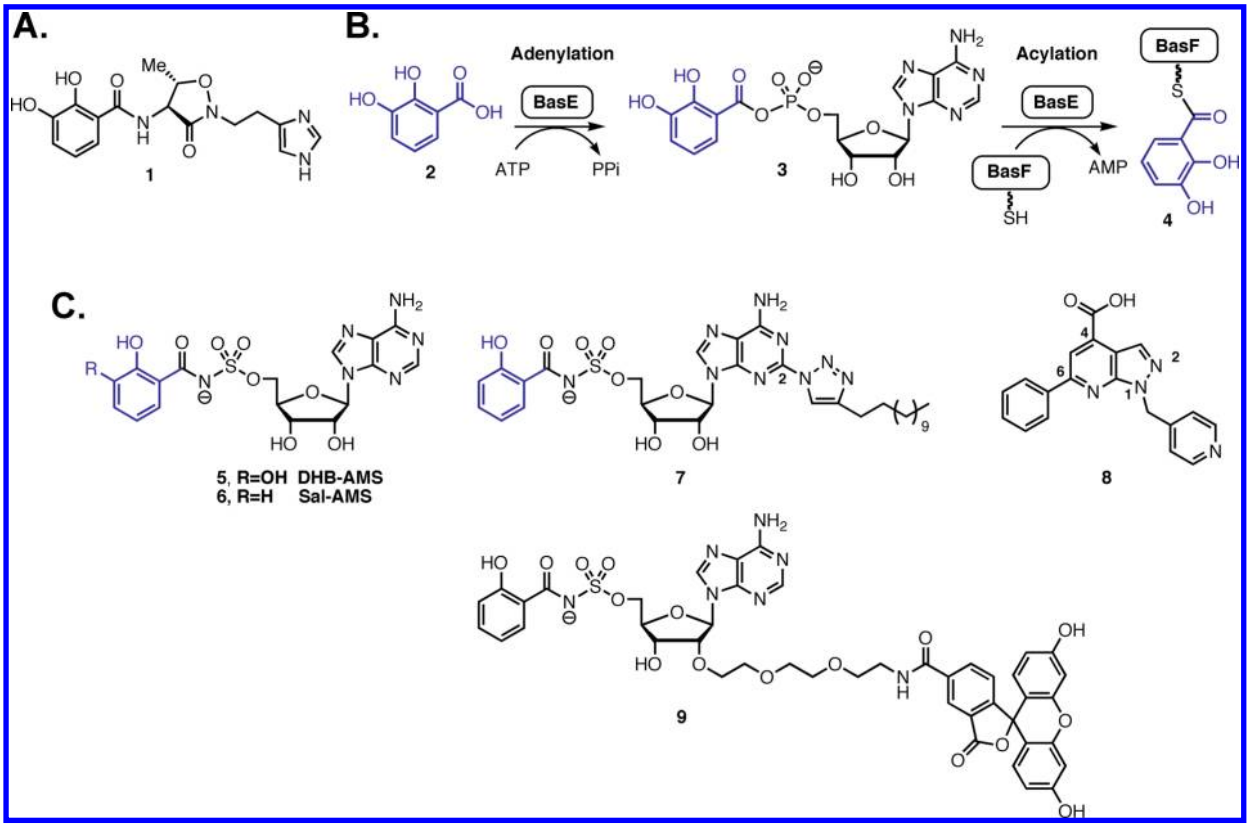


FIGURE 1: Synthetic steps for the production of acinetobactin. (A) Structure of acinetobactin produced by *A. baumannii*. The modified peptide is derived from one molecule each of 2,3-dihydroxybenzoate, threonine, and histidine. (B) The reaction catalyzed by the BasE adenylating enzyme. The two-step reaction involves the initial adenylation of DHB to form the aryl adenylate **3**. This intermediate is subsequently transferred to the pantetheine cofactor of the BasF aryl carrier protein. (C) Inhibitors of BasE have been identified through rational design (**5** or **7**) or screening (**8**). The inhibitor **8**, which was identified in a fluorescence polarization displacement assay with ligand **9**, is composed of three aromatic groups, the phenyl ring, the central pyrazolo[3,4-*b*]pyridine-4-carboxylate, and a 4-methylpyridyl moiety. Key atoms of inhibitors **7** and **8** are numbered for clarity.

protein (PCP), sometimes called a thiolation domain, that delivers the aminoacyl and peptidyl substrates to the respective catalytic domains. The PCP is posttranslationally modified by the activity of a phosphopantethienyl transferase that transfers a pantetheine moiety from a molecule of coenzyme A (*9*). The amino acid substrate is activated by the NRPS adenylation domain, which is therefore the primary specificity determining domain. Amino acids that have been loaded on the PCP domains of adjacent modules are joined by the activity of condensation domains, which catalyze peptide bond formation. These three domains, most commonly organized as condensation−adenylation−thiolation, serve as a complete extension unit for each NRPS module (*10*). Structural insights into the organization of these multidomain assemblies have been provided by the structure of a complete termination module (*11*).

The NRPS adenylation domain performs a two-step reaction, first catalyzing the attack of the amino acid carboxylate on the α-phosphate of ATP to form the adenylate intermediate and pyrophosphate. In a second reaction, the pantetheine thiol of the PCP displaces AMP to produce the acyl thioester. The adenylation domains belong to the ANL superfamily of acyl-adenylate forming enzymes that additionally includes acyl-CoA synthetases and firefly luciferases (*12*). Enzymes within this family contain two domains, a large N-terminal domain of 400−500 residues and a smaller C-terminal domain of ~110 residues. The active site is located at the interface between the two domains. The CoA binding site has been identified in three acyl-CoA synthetases (*13*−*15*) and contains a nucleotide binding site on the surface of the protein and a pantetheine tunnel that passes between the two domains to the active site. The pantetheine binding site of NRPS adenylation domains is likely to be very similar.

Structural and biochemical evidence (*14*, *16*−*20*) for members of this enzyme superfamily suggests the use of a *domain alternation* catalytic strategy for the overall ping-pong reaction. Upon completion of the initial adenylate-forming reaction, the C-terminal domain rotates by 140° to a new position that is used to catalyze the thioester-forming partial reaction (*12*).

The Gram-negative bacillus *Acinetobacter baumannii* has been identified as an increasingly common nosocomial pathogen (*2*, *21*, *22*). Numerous outbreaks have been observed in hospital settings across the globe. Even more worrisome is the degree to which multidrug resistant strains of *A. baumannii* are being encountered, including in military personnel in Iraq and Afghanistan (*23*). *A baumannii* uses a NRPS cluster for the synthesis of acinetobactin **1** (Figure 1), a peptidic siderophore (*24*−*27*). The aryl capping group on acinetobactin is derived from a molecule of 2,3-dihydroxybenzoate (**2**, DHB). This moiety is activated through the adenylating activity of BasE, which transfers the 2,3-dihydroxybenzoyl group to the pantetheine cofactor of the BasF aryl carrier protein domain (Figure 1B). Homologous self-standing adenylation domains (*28*) exist in the siderophore synthesis pathways of alternate pathogens, including VibE in vibriobactin synthesis in *Vibrio cholerae* (*29*), EntE of the enterobactin pathway of *Escherichia coli* (*30*), and MbtA of the mycobactin synthetic cluster of *Mycobacterium tuberculosis* (*31*, *32*).

Because of the role that siderophores play in the acquisition of iron (*5*), the inhibition of siderophore biosynthesis has been identified as a potential target for the development of novel antibacterial agents. The adenylating enzymes responsible for incorporation of the aryl capping group in siderophores have been targeted for rational design on the basis of the tight binding to the adenylate intermediate (**3**, Figure 1B). The stable adenylate mimics Sal-AMS **6** and DHB-AMS **5** (Figure 1C), which contain sulfamate linkages as isosteres of the labile phosphate moiety, have been described (*33*−*35*). Analysis of EntE demonstrates that **6** functions as a slow-onset inhibitor with picomolar inhibition and dissociation constants (*36*). Extensive structure−activity studies of these bisubstrate inhibitors have been performed with MbtA from *M. tuberculosis* to explore the impact of modifications to the aryl (*37*), linker (*34*, *38*), and nucleotide (*39*−*41*) moieties of Sal-AMS **6**. The unique binding mode of the adenylate in NRPS adenylation domains has also been utilized to design a conformationally restricted adenylation inhibitor that mimics the folded conformation of the intermediate adenylate (*42*). This inhibitor selectively inhibits NRPS adenylation enzymes and not the corresponding aminoacyl-tRNA synthetase, which binds the adenylate in an extended conformation.

These aforementioned inhibitors are all bisubstrate nucleoside mimics of the adenylate intermediate. These compounds may exhibit poor pharmacokinetic (PK) parameters because of their highly polar nature. In an effort to identify novel small molecule inhibitors with perhaps improved PK and cellular permeability, a high-throughput fluorescence polarization displacement assay was conducted with BasE from *A. baumannii*, which identified 6-phenyl-1-(pyridin-4-ylmethyl)-1*H*-pyrazolo[3,4-*b*]pyridine-4-carboxylic acid **8** as a potent inhibitor with a $K_D$ of 78 nM (Figure 1C) (*43*).

Herein we report the functional and structural characterization of BasE. The ability of BasE to transfer activated 2,3-dihydroxybenzoic acid in *trans* onto the cognate aryl carrier protein (ArCP) domain of BasF was characterized using a continuous coupled assay and via mass spectrometry of the acylated BasF protein. Initial velocity studies were used to measure the kinetic parameters for the native substrates DHB, ATP, and holo-BasF as well as several non-native aryl acids in the BasE reaction. Next, the modality of inhibition for **8** was performed with respect to both substrates DHB and ATP. Finally, we determined the crystal structure of BasE derived from a clinical strain of *A. baumannii* bound to the bisubstrate inhibitors 5′-*O*-[*N*-(2,3-dihydroxybenzoyl)sulfamoyl]adenosine **5**, 2-(4-*n*-dodecyl-1,2,3-triazol-1-yl)-5′-*O*-[*N*-(2-hydroxybenzoyl)sulfamoyl]-adenosine **7**, which is an analogue of **5** modified at the C2 position of the adenine base, and inhibitor **8** derived from high-throughput screening. Compound **8** bound in an unexpected binding mode in which the C-6 phenyl group is in the pantetheine tunnel. The structural insight from these studies has enabled further optimization of the pyrazolo[3,4-*b*]pyridine scaffold in **8** to enhance binding affinity by taking advantage of the additional interactions through modification of the C-6 phenyl group. These structural studies also revealed how the bulky C2 substituent of bisubstrate inhibitor **7**, which is essential for antibacterial activity, is accommodated.

## MATERIALS AND METHODS

*Materials*. Inhibitors **5** (*37*) and **7** (*41*) were prepared as described; **8** was purchased from Enamine (Ukraine). Chemically competent *E. coli* BL21 STAR (DE3) were purchased from Invitrogen (Carlsbad, CA, USA). Restriction enzymes were supplied by New England Biolabs (Ipswich, MA, USA). Primers for PCR were obtained from Integrated DNA Technologies (Coralville, IA, USA). Expression vectors were purchased from EMD Biosciences (San Diego, CA, USA). Nickel nitrilotriacetic acid (Ni-NTA) was obtained from Fisher Scientific (Pittsburgh, PA, USA). IPTG was purchased from Gold BioTechnology (St. Louis, MO, USA). MesG was obtained from Berry & Associates (Dexter, MI, USA). The pET15bTEV plasmid and TEV protease were described previously (*44*). All other chemicals, biological buffers, and the coupling enzymes inorganic pyrophosphatase (I1643) and purine nucleoside phosphorylase (N8264) were purchased from Sigma-Aldrich (St. Louis, MO, USA).

*Cloning, Expression, and Purification of BasE from A. baumannii AB900*. The genes encoding BasE proteins from two different strains of *A. baumannii* were independently cloned for this study. The proteins share 97.5% sequence identity. The *basE* gene from *A. baumannii* strain AB900, a clinical isolate (*45*), was cloned by PCR using primers designed to incorporate restriction sites at the 5′ (*Nde*I) and 3′ (*Xho*I). A 1.6 kb fragment was amplified and subcloned into the pET15bTEV plasmid (*44*) for protein expression and purification. The gene was sequenced and compared to the sequence deposited for the AB900 clinical strain to confirm accurate amplification. The NCBI accession code for BasE from this strain is ZP_04661818. The plasmid pET15bTEV-basE, pED453, was transformed into BL21(DE3) cells for protein expression. Cells were grown in LB to an $OD_{600}$ of ∼0.6 at 37 °C. Protein expression was induced by the addition of 0.75 mM IPTG to the media, and the cells were incubated overnight at 16 °C. The cells were harvested by centrifugation at 4800*g* for 20 min. Subsequent purification steps were performed at 4 °C. The cells were lysed with a microfluidizer (M-110EH Microfluidizer; Microfluidics Corp., Newton, MA) using a lysis buffer containing 50 mM Tris (pH 7.5), 150 mM NaCl, 10 mM imidazole, and 0.2 mM TCEP. Membrane fractions, nucleic acid, and unlysed cells were removed by centrifugation at 45000 rpm for 45 min. The cell lysate was applied to a His-trap (GE Healthcare) IMAC column; weakly bound proteins were removed with lysis buffer containing 50 mM imidazole. BasE was eluted with lysis buffer containing 300 mM imidazole. For removal of the protein tag, the protein was dialyzed against cleavage buffer [50 mM Tris (pH 8.0), 150 mM NaCl, 0.2 mM TCEP, 0.5 mM EDTA], and TEV protease was added to BasE at a molar ratio of ∼1:80. Cleavage was allowed to proceed for 18 h within the dialysis bag. The protein was then clarified and passed over the His-trap column a second time to remove uncleaved BasE, TEV protease, and the cleaved 18 amino acid His-tag sequence. The protein in the column flow-through was collected and dialyzed against crystallization buffer [10 mM HEPES (pH 7.5), 25 mM NaCl, 0.2 mM TCEP]. The final protein was concentrated to ∼20 mg/mL using an extinction coefficient at 280 nm of 46040 $M^{-1}$ $cm^{-1}$.

*Expression and Purification of BasE from A. baumannii ATCC17978*. The previously described pET28b plasmid encoding the *basE* gene from *A. baumannii* strain ATCC17978 was transformed into competent *E. coli* BL21(DE3) cells (*43*). BasE was overexpressed as an N-terminal His-tagged protein and purified as described (*43*). The NCBI accession code for BasE from the ATCC strain is ABO12800. Unless otherwise noted, kinetic studies were performed with the BasE protein from ATCC17978 while the crystallographic experiments used BasE protein from strain AB900.

*Cloning, Expression, and Purification of BasF from A. baumannii AB900*. The *basF* gene was PCR amplified from genomic DNA purified from *A. baumannii* strain AB900 using the same strategy described above for the *basE* gene using *Nde*I (5′) and *Bam*HI (3′) restriction sites incorporated into the amplified gene. The NCBI accession code for BasF from *A. baumannii* strain AB900 is ZP_04661817. The pET15bTEV plasmid harboring *basF* was transformed into competent *E. coli* BL21(DE3) cells. A 100 mL preculture (15 mL diluted to 1 L) was used to inoculate 4 × 1 L of LB broth media containing ampicillin (100 μg/mL). After being shaken at 37 °C to an $OD_{600}$ of 0.6, the culture was induced with 0.75 mM IPTG and grown for an additional 4 h at 28 °C. Cells were harvested, resuspended in 50 mL of lysis buffer [50 mM HEPES (pH 8.0), 300 mM NaCl, 10 mM imidazole], and sonicated using a Branson sonifier 250 at 0 °C with three 2 min bursts (power 7, 30% duty cycle) with a 1 min break between each burst. The lysate was cleared by centrifuging at 45000*g* for 10 min at 4 °C. A suspension of 50% Ni-NTA (10.0 mL) was added to the cleared supernatant, and the resulting mixture was gently incubated end over end for 1 h at 4 °C. The suspension was loaded into an empty column, and the flow-through was collected. The resin was then washed with 40 mL of wash buffer [50 mM HEPES (pH 8.0), 300 mM NaCl, 20 mM imidazole] and eluted with 30 mL of elution buffer [50 mM HEPES (pH 8.0), 300 mM NaCl, 250 mM imidazole]. Fractions containing BasF were pooled and desalted on a PD-10 column (GE Healthcare) into phosphopantetheinylation buffer (20 mM Tris, pH 7.5).

*Phosphopantetheinylation of BasF*. Sfp phosphopantetheinyl transferase was purified as described previously (*46*). Sfp (4.0 μM) was incubated with apo-BasF (200 μM) and CoA (200 μM) in 20 mM Tris, pH 7.5, containing 10 mM $MgCl_2$ for 1 h at 25 °C (*36*). ESI-TOF mass spectrometry confirmed complete phosphopantetheinylation of BasF. Holo-BasF was purified on a Mono Q 5/50 GL column (GE Healthcare) using the binary buffers system A (20 mM Tris, pH 8.0) and system B (50 mM Tris, pH 8.0, 1.0 M NaCl) and a 40 column volume gradient from 0% to 100% B over 40 min at 1.0 mL/min. Holo-BasF eluted at approximately 28 mS/cm, and fractions containing pure holo-BasF were pooled and concentrated to afford 13 mg of purified protein/L of culture. An extinction coefficient at 280 nm of 58560 $M^{-1}$ $cm^{-1}$ was used to determine protein concentration.

*Enzyme Activity Assay*. Kinetic assays studying the full BasE acylation reaction were run under initial velocity conditions (typically 2−5 min) using the MesG coupled enzyme assay (EnzChek pyrophosphate assay; Invitrogen) with 10 nM BasE, 50 mM Tris (pH 8.0), 5.0 mM $MgCl_2$, 0.5 mM DTT, 0.1 unit of nucleoside phosphorylase, 0.04 unit of pyrophosphatase, 0.2 mM MesG, and varying concentrations of BasF, DHB, and ATP. The concentration of BasE was increased to 30 nM for analysis with the substrates 3-hydroxybenzoic acid (3-HBA) and benzoic acid (BA). Reactions (70 μL) were run in 96-well half-area UVStar plates (Greiner), and formation of 7-methyl-6-thioguanine was measured at 360 nm ($\varepsilon_{360}$ = 11000 $M^{-1}$ $s^{-1}$) at 25 °C on a Molecular Devices SpectraMax M5e. Steady-state kinetic parameters of the substrates (BasF, ATP, DHB, SAL, 3-HBA, and BA) were determined by measuring the initial velocity as a function of substrate concentration at saturating concentrations of the nonvaried substrates to provide a saturation curve that was fit by nonlinear regression analysis to eq 1 using Graphpad Prism 4.0:

$$v = (VA)/(K + A) \quad (1)$$

where $V$ is the maximal velocity, $A$ is the substrate concentration, and $K$ is the Michaelis−Menten constant ($K_M$). Studies to confirm that the reaction rate was linearly dependent on BasE concentration in this coupled enzyme assay employed BasE from 5−40 nM while BasF, DHB, and ATP concentrations were held at 50 μM, 250 μM, and 2.5 mM, respectively. Kinetic parameters for BasF were determined at fixed concentrations of DHB (250 μM) and ATP (2.5 mM) and at varying concentrations of BasF (1−100 μM). Kinetic constants for DHB were determined at fixed concentrations of BasF (50 μM) and ATP (2.5 mM) and at varying concentrations of DHB (2.5−50 μM). Kinetic parameters for ATP were determined at fixed concentrations of BasF (50 μM) and DHB (250 μM) and at varying concentrations of ATP (0.05−2.0 mM). Kinetic constants for the non-native aryl acid substrates were determined at fixed concentrations of BasF (10 μM) and ATP (2.5 mM) and at varying concentrations of the respective substrate: 5−250 μM for salicylic acid, 0.4−100 μM for 3-hydroxybenzoic acid, and 31−2000 μM for benzoic acid. For all experiments, a blank reaction was performed wherein the aryl acid substrate was omitted from the reaction for background subtraction.

*Mass Spectrometry Analysis of BasF*. Apo-BasF, holo-BasF, and acylated holo-BasF were analyzed by ESI-TOF mass spectrometry (QSTAR; Applied Biosystems). Apo- and holo-BasF proteins (50 μM) were prepared in buffer consisting of 50 mM Tris (pH 8.0), 5.0 mM $MgCl_2$, 2.5 mM ATP, and 0.5 mM DTT. Acylated holo-BasF protein was prepared by incubating 50 μM holo-BasF with 200 nM BasE and 250 μM aryl acid (DHB, SAL, 3-HBA, BA) in buffer consisting of 50 mM Tris (pH 8.0), 5.0 mM $MgCl_2$, 2.5 mM ATP, and 0.5 mM DTT in a total reaction volume of 25 μL and incubated 16 h. One microliter of the reaction mixture was diluted to 500 μL with 50:50 water: acetonitrile containing 0.1% formic acid; 10 μL of this solution was directly injected onto the ESI-TOF MS instrument.

*Kinetic Inhibition Experiments*. The continuous coupled assay described above was used to measure enzyme inhibition. Varying concentrations of inhibitor (136× DMSO stock) providing a final DMSO concentration of 0.74% (*v*/*v*) or DMSO only (control) were preincubated with the master mix containing BasE but lacking the varied substrate for 10 min at 25 °C, followed by addition of varying concentrations of ATP or DHB to initiate the reaction. As opposed to the bisubstrate analogues **5**−**7**, compound **8** did not exhibit slow binding inhibition (data not shown). For experiments studying the mode of inhibition with respect to ATP, DHB was held constant at 250 μM while varying ATP (0, 0.15, 0.3, 0.45, 1.2, 2.5 mM) and inhibitor **8** (0, 19.1, 57.3, 147 μM). For experiments studying the mode of inhibition with respect to DHB, ATP was held constant at 2.5 mM while varying DHB (0, 4, 6, 12, 40, 250 μM) and inhibitor **8** (0, 0.8, 2.4, 7.2 μM). The resulting initial velocity data were fit to competitive, uncompetitive, noncompetitive, and mixed models of inhibition using the enzyme kinetics module of SigmaPlot, and the model with the highest AICc value was selected to provide $K_i^{app}$ values with respect to the varied substrate at a fixed concentration of the nonvaried substrates. Based on the inhibition studies, which shows **8** is competitive with respect to both DHB and ATP, estimates of the intrinsic $K_i$ values of **8** were determined using eq 2:

$$K_i^{app} = K_i(1 + A/K_{ia}) \quad (2)$$

where $K_i$ is the true inhibition constant for **8**, $K_i^{app}$ is the apparent inhibition constant with respect to ATP at a fixed saturating concentration of DHB, $A$ is the concentration of the nonvaried

substrate DHB, and $K_{ia}$ is the dissociation constant for the nonvaried substrate DHB, which was previously determined as 2.63 $\mu$M (*43*).

*Fluorescence Polarization Binding Assay*. The binding affinity of BasE isoforms from *A. baumannii* ATCC17978 and AB900 were determined using 2′-*O*-{2-[2-(2-{[(fluorescein-5-yl)-carbonyl]amino}ethoxy)ethoxy]ethoxy}-5′-*O*-[*N*-(2-hydroxybenzoyl)sulfamoyl]adenosine (Fl-Sal-AMS, **9**), which is a fluorescein-labeled derivative of **6**, in a fluorescence polarization displacement assay, as described previously (*43*).

*Crystallization and Structure Determination*. The BasE protein was screened for crystallization conditions using sparse matrix screening methods (*47*). BasE crystals were optimized from leads first identified from an in-house sparse matrix screen. Crystals of the native protein were grown at 14 °C by hanging drop vapor diffusion using a 1:1 mixture of protein and precipitant containing 5−15% PEG 8000, 5% MPD, 250−600 mM $CaCl_2$, and 50 mM BTP (pH 7.5). Native crystals were mounted in nylon loops and cryoprotected by transferring through three solutions containing increasing amounts of ethylene glycol (8%, 16%, 24%) for approximately 30 s each and stored in liquid nitrogen. The final cryoprotectant solution contained 24% MPD, 15% PEG 8000, 0.6 M $CaCl_2$, and 50 mM BTP (pH 7.5).

BasE was also cocrystallized with **5**, **7**, and **8**. Inhibitor **5** was dissolved in $H_2O$ at a concentration of 50 mM. Compound **7** was dissolved in 50% methanol to a concentration of 20 mM. Finally, **8** was dissolved in 50% methanol to 7.5 mM. Ligands were incubated with the protein at 1.5× molar excess over protein for 45 min on ice prior to crystallization. Crystals were grown in the same manner as described for the unliganded BasE protein, and cryoprotection was similar with the addition of 0.5 mM ligand at each of the three steps.

An initial 2.7 Å data set was collected on a RU300-HR home X-ray source. Crystals were indexed to a primitive orthorhombic space group with unit cell $a$ = 66.3 Å, $b$ = 143.4 Å, and $c$ = 149.0 Å. Analysis of the systematic absences identified the space group as $P2_12_12_1$. The data set from the home source had an overall $R_{merge}$ of 0.135, 98% completeness, and $I/\sigma$ of 10.1. Values for the highest resolution shell were 0.49%, 95%, and 2.3%, respectively. Matthews' coefficient analysis suggested two molecules (57% solvent) were likely present in the asymmetric unit.

We initially tried to solve the structure of BasE using MOLREP (*48*) with the protein atoms from the full-length structure of DhbE (1MDB) as a search model. A solution was found that contained a single protein chain; a second chain, expected from Matthews' analysis, could not be found. Not knowing which of the two C-terminal conformations would be found, we repeated the molecular replacement search with a DhbE model of only the N-terminal domain that was modified with CHAINSAW (*49*) to remove nonconserved side chains. Molecular replacement was performed with PHASER (*50*) and the N-terminal domain model, and two chains were found in the asymmetric unit. An initial cycle of refinement of this solution with REFMAC (*51*) resulted in a *R*-factor of 35% (*R*-free of 40%). Further refinement and manual model building resulted in crystallographic and free *R*-factors of 23.8% and 28.3% with no solvent molecules incorporated into the model; electron density for the C-terminal domain was not apparent.

The molecular model from the in-house data set was not refined to completion but served as the starting model for refinement of subsequent synchrotron data sets. We collected a 2.7 Å data set of a crystal obtained from protein cocrystallized with DHB-AMS **5**. The data were collected remotely using the BLU-ICE software (*52*) at SSRL beamline 9-1. A second data set was collected for a crystal obtained in the presence of **7** at SSRL

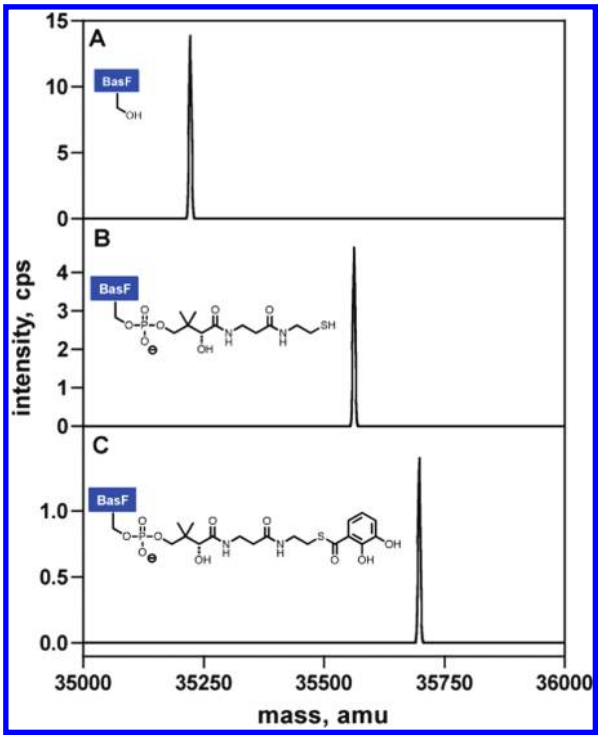


FIGURE 2: Deconvoluted MS spectra of apo-BasF (A), holo-BasF (B), and acylated BasF (C). Sfp was used to convert apo-BasF to holo-BasF. To arylate holo-BasF with DHB, 200 nM BasE was used, and the reaction was allowed to proceed overnight at room temperature.

Table 1: Mass Spectrometry Studies of Apo-, Holo-, and Aryl Acid-Loaded BasF

| protein species | acid substrate[a] | loading | expected mass (Da) | deconvoluted mass (Da) |
|---|---|---|---|---|
| apo-BasF | | | 35222.6 | 35222.1 |
| holo-BasF | | | 35562.6 | 35562.4 |
| holo-BasF | DHB | full | 35698.7 | 35698.0 |
| holo-BasF | SAL | partial | 35682.7 | 35682.2 |
| holo-BasF | 3-HBA | partial | 35682.7 | 35682.4 |
| holo-BasF | BA | partial | 35666.7 | 35666.3 |

[a]DHB = 2,3-dihydroxybenzoic acid, SAL = salicylic acid/2-hydroxybenzoic acid, 3-HBA = 3-hydroxybenzoic acid, and BA = benzoic acid.

Table 2: Kinetic Parameters of BasE[a]

| substrate[b] | $K_M$ ($\mu$M) | $k_{cat}$ ($s^{-1}$) | $k_{cat}/K_M$ ($M^{-1}$ $s^{-1}$) |
|---|---|---|---|
| DHB | 4.01 ± 1.41 | 2.6 ± 0.3 | $6.5 \times 10^5$ |
| ATP | 300 ± 71 | 2.8 ± 0.2 | $9.3 \times 10^3$ |
| BasF | 9.80 ± 1.35 | 3.1 ± 0.1 | $3.2 \times 10^5$ |
| SAL | 7.55 ± 0.96 | 0.9 ± 0.1 | $1.2 \times 10^5$ |
| 3-HBA | 3.28 ± 0.60 | (4.5 ± 0.6) × $10^{-2}$ | $1.4 \times 10^4$ |
| BA | 301 ± 32 | (1.5 ± 0.2) × $10^{-1}$ | $5.0 \times 10^2$ |

[a]Initial velocities of the BasE reaction were assayed spectrophotometrically using the coupled assay as described in Materials and Methods. All assays were performed at 25 °C and pH 8.0. [b]DHB=2,3-dihydroxybenzoic acid, SAL = salicylic acid/2-hydroxybenzoic acid, 3-HBA = 3-hydroxybenzoic acid, and BA = benzoic acid.

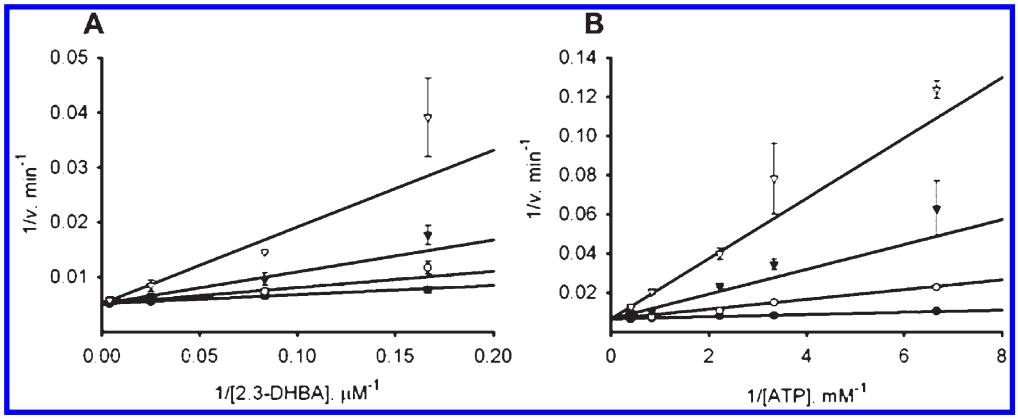


FIGURE 3: Inhibition of BasE with inhibitor **8**. (A) Initial velocity data of variable amounts of inhibitor (0 $\mu$M (●), 0.73 $\mu$M (○), 2.4 $\mu$M (▼), 7.2 $\mu$M (▽)) and DHB at a fixed concentration of ATP (2.5 mM). (B) Initial velocity data of variable amounts of inhibitor (0 $\mu$M (●), 19.1 $\mu$M (○), 57.3 $\mu$M (▼), 147 $\mu$M (▽)) and ATP at a fixed concentration of DHB (250 $\mu$M). The inhibitor is competitive with respect to both substrates, with $K_i^{DHB} = 1.0 \pm 0.2$ $\mu$M and $K_i^{ATP} = 5.6 \pm 1.0$ $\mu$M.

beamline 11-1. The **7** crystal diffracted to 1.9 Å. Finally, a 2.1 Å data set was collected at Cornell High Energy Synchrotron Source beamline A1 for a crystal of BasE grown in the presence of **8**. The crystal bound to **8** was annealed by blocking the $N_2$ stream for 3 s prior to data collection.

The structures of all three liganded complexes were determined by difference Fourier methods. At each stage, the starting model for refinement was derived from the protein atoms of the highest resolution model that was available; all solvent, additive, or ligand atoms were removed from the initial model.

The model derived from the in-house data served as the starting coordinate file for determining the DHB-AMS **5** structure. Subsequently, the protein atoms from the model of the DHB-AMS structure were used to provide initial phases for the **8** structure. And finally, the protein atoms from the **8** structure served as the starting model for calculating phases of the **7** data set. Clear electron density was observed for all inhibitors; a portion of the aliphatic tail of **7** is disordered. Iterative model building with COOT (*53*) and refinement with REFMAC5 (*51*) were continued to completion. As described below, electron density for the entire C-terminal domain was missing from the structures.

## RESULTS AND DISCUSSION

*Sequence Analysis of the BasE Adenylation Enzyme*. The BasE sequence was compared to homologous proteins in the siderophore synthetic pathways of other organisms. The BasE protein is 36.7% identical to MbtA of *M. tuberculosis* (*32*), 43.4% to DhbE of *Bacillus subtilis* (*54*), and 55.5% to EntE from *E. coli* (*55*).

There are currently genome sequences of seven *A. baumannii* strains (*45*, *56*, *57*). The pairwise identities of the BasE proteins from any two strains range from 97% to 100%. Of the 542 residues of BasE, 519 (96%) are conserved at the level of identity in all seven strains. The differences are roughly equally distributed between the multiple strains and therefore do not appear to be clear subpopulations of sequences. There are no deviations at the 10 conserved regions identified for the NRPS adenylation domains and larger ANL superfamily of enzymes (*12*, *58*). The sequences of the two BasE proteins used in this study differed at seven positions. All of the substitutions are more than 20 Å from the active site except for residue 362, which is a cysteine in the BasE from ATCC17978 and an arginine in AB900. This residue, however, is located on the surface and points away from the active site.

*Cloning, Expression, and Purification of BasE and Apo-BasF*. The *basE* and *basF* genes were PCR amplified from *A. baumannii* strain AB900 genomic DNA and cloned into a modified pET15b vector containing a TEV cleavage site and an N-terminal His tag. DNA sequencing of the cloned fragments confirmed the expected sequence and the absence of any mutations. Overexpression was performed in *E. coli* Rosetta(DE3)2 cells harboring each overexpression construct, and purification of soluble protein was performed via His-Trap affinity chromatography using standard binding, washing, and elution to afford 47 mg of BasE and 27 mg of apo-BasF per liter of culture. For crystallography studies of BasE, the 18 amino acid N-terminal His-tag sequence was removed by treatment with TEV protease. The molecular mass of native BasE determined by SDS−PAGE was ~63 kDa, consistent with the molecular mass of 62872 Da calculated from the amino acid sequence of BasE from AB900. The molecular mass of apo-BasF determined by SDS−PAGE was ~35 kDa, consistent with the molecular mass of 35222 Da calculated from the amino acid sequence of BasF from *A. baumannii* AB900 and the histidine tag.

*Phosphopantetheinylation of BasF*. BasF is a multifunctional 281 amino acid protein containing an N-terminal isochorismatase domain (residues 1−206) and a C-terminal aryl carrier protein (ArCP) domain (residues 218−281) (*25*). The ArCP domain contains a conserved serine residue (Ser246 in BasF) to which a phosphopantetheine molecule is covalently attached. The terminal thiol of the phosphopantetheine moiety is the site of substrate loading. Activation of carrier proteins occurs post-translationally via addition of phosphopantetheine from coenzyme A catalyzed by a phosphopantetheinyl transferase (PPTase). The gene product of *basI* located in the acinetobactin gene cluster encodes for a putative phosphopantetheinyltransferase (*25*). However, we used the promiscuous PPTase from *Bacillus subtilis* encoded by *sfp* for the in vitro phosphopantetheinylation of apo-BasF. Sfp was overexpressed and purified as previously described (*46*). Incubation of purified apo-BasF and coenzyme A with Sfp resulted in the complete conversion to holo-BasF as determined by electrospray-time-of-flight (ESI-TOF) mass spectrometry (Figure 2A,B). The deconvoluted masses of apo-BasF (35222 Da) and holo-BasF (35562 Da) corresponded to the expected masses of these proteins (Table 1). Holo-BasF was subsequently purified by ion-exchange chromatography on a Mono

Q 5/50 GL column to afford 13 mg of purified holo-BasF protein/L of culture. This final purification step was crucial to remove impurities that resulted in an extremely high background signal in the subsequent coupled enzyme assay.

*Steady-State Kinetic Studies*. As a prelude to detailed structural studies, we determined the steady-state kinetic parameters for the three substrates of the BasE reaction using a continuous coupled assay, which measures release of pyrophosphate in the adenylation half-reaction. Pyrophosphate was hydrolyzed to inorganic phosphate by inorganic pyrophosphatase, and phosphate production was coupled to phosphorolysis of 7-methyl-6-thioguanosine (MesG) catalyzed by the enzyme purine nucleoside phosphorylase, and the chromogenic product, 7-methyl-6-thioguanine, was monitored by absorbance at 360 nm. We confirmed that the reaction rate was linearly dependent on BasE concentration for this coupled assay system. Initial velocity experiments provided $K_M$ values of 4.0, 300, and 9.8 $\mu$M for DHB, ATP, and holo-BasF, respectively, with an average $k_{cat}$ equal to 2.8 $s^{-1}$ (Table 2). For each saturation experiment, one substrate was varied while the other two substrates were held at fixed saturating concentrations. The $k_{cat}$ value is equivalent to the $k_{cat}$ for the analogous *E. coli* adenylating enzyme, EntE, involved in the synthesis of the prototypical siderophore known as enterobactin. Furthermore, the $K_M$ values for the three substrates with BasE were also commensurate to values for the analogous substrates measured with EntE (*36*). For comparison, the classic ATP−$PP_i$ exchange assay of BasE with DHB, which only measures the adenylation half-reaction, provided values for $k_{cat}$ and $K_M$ of 3.5 $s^{-1}$ and 1.5 $\mu$M, respectively, at saturating concentrations of ATP (*43*). We also directly confirmed acylation of holo-BasF by BasE using ESI−TOF mass spectrometry. As shown in Figure 2C, BasE catalyzed the complete conversion of holo-BasF to DHB-holo-BasF, with the deconvoluted mass corresponding to the expected mass (Table 1).

We next probed the substrate specificity of BasE by measuring the kinetic parameters with other aryl acid substrates (Table 2). Salicylic acid (SAL, 2-hydroxybenzoic acid) was also an excellent substrate with a specificity constant approximately 6-fold lower than DHB due to an approximately 2- and 3-fold attenuation in $K_M$ and $k_{cat}$ values, respectively, relative to DHB. The regioisomeric substrate 3-hydroxybenzoic acid (3-HBA) was found to have a 46-fold lower specificity constant, due exclusively to a decrease in the $k_{cat}$ value. These results suggest the 2-hydroxy group of DHB is more important than the 3-hydroxy group for catalytic efficiency. To complete our cursory substrate specificity study, benzoic acid was evaluated and found to possess a 3 orders of magnitude decrease in specificity constant that is attributed to an approximate 100-fold increase in $K_M$ and 10-fold decrease of $k_{cat}$ relative to DHB. We also confirmed that all substrates were successfully loaded onto holo-BasF by ESI-TOF mass spectrometry. Under the same conditions as used for DHB, only partial loading (~70%) of the non-native aryl acids was observed (Table 1).

*Inhibition and Binding of **8** to BasE*. The bisubstrate inhibitors SAL-AMS **6** and DHB-AMS **5** are slow tight-binding

Table 3: Ligand−Protein Dissociation and Inhibition Constants[a]

| inhibitor/probe | assay[b] | BasE-ATCC ($\mu$M) | BasE-AB900 ($\mu$M) |
|---|---|---|---|
| **8** | FP | 0.078 ± 0.007 | 0.058 ± 0.011 |
| | ITC | 0.099 ± 0.013 | ND[c] |
| | kinetic | 0.058 ± 0.011 | ND[c] |
| **9** | FP | 0.084 ± 0.006 | 0.144 ± 0.009 |

[a]Dissociation and inhibition constants of **8** and **9** with BasE derived from *A. baumannii* strain AB900 or ATCC17978. [b]FP, $K_D$ determined by fluorescence polarization displacement assay (*43*); ITC, $K_D$ determined by isothermal titration calorimetry (*43*); kinetic, $K_i$ value derived from eq 2 using the spectrophotometric assay described in the text. [c]Not determined.

Table 4: Crystallographic Diffraction and Refinement Data

| | BasE + **5** | BasE + **7** | BasE + **8** |
|---|---|---|---|
| beamline | SSRL 9-1 | SSRL 11-1 | CHESS A-1 |
| resolution (Å) | 40.0−2.7 | 40.0−1.9 | 30.0−2.1 |
| space group | $P2_12_12_1$ | $P2_12_12_1$ | $P2_12_12_1$ |
| unit cell | | | |
| *a* (Å) | 65.4 | 66.4 | 65.5 |
| *b* (Å) | 145.3 | 144.3 | 143.3 |
| *c* (Å) | 149.1 | 148.5 | 148.8 |
| $R_{merge}$[a] (%) | 13.1 (38.0) | 8.5 (42.3) | 7.2 (42.5) |
| completeness[a] (%) | 97.5 (88.6) | 93.8 (68.8) | 99.7 (97.9) |
| $I/\sigma$[a] | 9.2 (2.2) | 9.5 (1.8) | 10.8 (1.8) |
| no. of observations | 148782 | 402625 | 330221 |
| no. of reflections | 32168 | 106833 | 82475 |
| $R_{cryst}$ (overall/highest resolution shell)[a] (%) | 20.0 (27.6) | 19.4 (29.4) | 18.5 (26.5) |
| $R_{free}$ (overall/highest resolution shell)[a] (%) | 25.1 (37.1) | 21.7 (30.3) | 21.0 (31.4) |
| Wilson *B*-factor (Å$^2$) | 56.6 | 21.9 | 32.3 |
| average *B*-factor, protein[b] (Å$^2$) | | | |
| A (Å$^2$) | 42.2 | 27.0 | 35.3 |
| B (Å$^2$) | 42.7 | 25.9 | 35.1 |
| average *B*-factor, ligand, solvent, ions (Å$^2$) | 30.6, 32.1, 49.7 | 21.4, 30.8, 34.6 | 28.9, 39.7, 36.8 |
| no. of water molecules, $Ca^{2+}$ ions | 45, 4 | 504, 5 | 431, 4 |
| rms deviation | | | |
| bond lengths (Å) | 0.017 | 0.010 | 0.010 |
| angles (deg) | 1.71 | 1.24 | 1.18 |

[a]Values for the highest resolution shell (2.8−2.7 Å for **5** and 2.2−2.1 Å for **8**) are given in parentheses. [b]The two numbers refer to average *B*-factors for chains A and B, respectively.

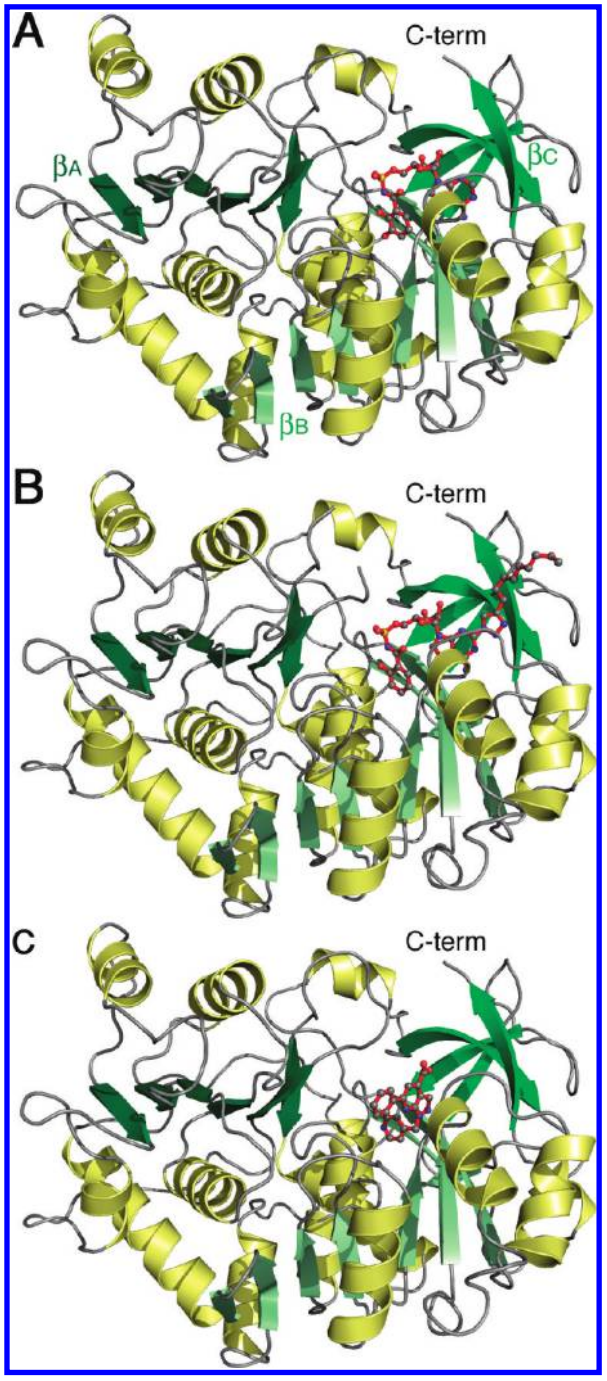


FIGURE 4: Structure of the BasE N-terminal domain bound to inhibitors. Ribbon diagram of BasE bound to (A) DHB-AMS **5**, (B) compound **7**, and (C) compound **8**. The three $\beta$-sheets of the N-terminal domain are labeled $\beta$A, $\beta$B, and $\beta$C in panel A, according to the nomenclature introduced for the phenylalanine activating domain of GrsA, an adenylation domain involved in gramicidin synthesis. The position of the C-terminal domain is indicated above Lys437, the hinge residue positioned between the N- and C-terminal domains. The ligands are shown with red bonds, gray carbon atoms, blue nitrogen atoms, red oxygen atoms, and yellow sulfur atoms.

picomolar inhibitors, whose binding affinity is driven almost exclusively by enthalpic interactions as determined with EntE, which also catalyzed the activation of DHB and covalent thioesterification onto a downstream aryl carrier protein (ArCP) domain (*36*). By contrast, the binding mode of the small molecule inhibitor **8**, which was identified from HTS, was unknown at the onset of these studies. To gain insight into inhibitor binding of **8**, we next performed kinetic studies using the continuous coupled assay described above to determine the modality of inhibition of **8** with respect to both DHB and ATP. In these experiments, the initial velocity was measured as a function of **8** at varying concentrations of either DHB or ATP with the second substrate held at a saturating fixed value. As shown in Figure 3, **8** displayed competitive inhibition with respect to DHB, providing a $K_i^{app}$ of 1.0 $\mu$M at a fixed saturating concentration of ATP (2.5 mM). Inhibitor **8** also showed competitive inhibition with respect to ATP, providing a $K_i^{app}$ of 5.6 $\mu$M at a fixed saturating concentration of DHB (250 $\mu$M). We also confirmed that **8** (200 $\mu$M) did not inhibit the coupling enzymes used in the continuous assay (data not shown). The finding that **8** exhibited competitive inhibition with respect to both substrates demonstrates that this small molecule inhibitor must occupy both substrate binding pockets. The intrinsic $K_i$ was estimated using the analysis of Blanchard and co-workers for bisubstrate inhibitors to provide a $K_i$ value of 0.058 $\mu$M as detailed in Materials and Methods (*59*). This value agrees closely with the dissociation constant ($K_D$) of 0.099 $\mu$M as determined using isothermal titration calorimetry and the $K_D$ value of 0.078 $\mu$M as measured in a fluorescence polarization displacement assay (FP) (*43*). The subsequent structural studies employed BasE from strain AB900; thus we also confirmed that **8** bound to this protein with essentially equal affinity as measured by FP, providing a $K_D$ of 0.058 $\mu$M (Table 3).

*Structure Determination of BasE from A. baumannii AB900*. BasE crystallized in the orthorhombic space group with Matthews' analysis suggesting that two molecules were present in the asymmetric unit. Molecular replacement using the N-terminal domain (residues 1−430) of DhbE as a search model gave a solution with two molecules in the asymmetric unit. Surprisingly, initial electron density maps failed to show any density beyond Lys437, the hinge between the two domains. Subsequent higher resolution data sets all failed to illustrate any density for the C-terminal domain.

The BasE protein was cocrystallized with three inhibitors, DHB-AMS **5**, **7**, and **8** (Figure 1C), using conditions that were similar to those of the unliganded protein, and crystals were used for data collection at synchrotron radiation sources (Table 4). The molecular models were refined against these data (Figure 4). Protein crystals were washed, dissolved, and analyzed by SDS−PAGE, demonstrating that the protein was intact and was not proteolytically cleaved to the N-terminal domain alone (data not shown). Prior structures of the ANL enzymes have also demonstrated significant crystallographic disorder in the C-terminal domain. In 1V26, the structure of the fatty acyl-CoA synthetase from *Thermus thermatoga* (*60*), for example, chain A is missing 46 of 107 residues in the C-terminal domain, and chain B is missing 24 residues. Additionally, structures of enzymes of this family determined by numerous investigators demonstrate significantly higher *B*-factors for C-terminal residues: firefly luciferase (*61*) has *B*-factor values of 24.0 and 43.1 Å$^2$ for the N- and C-terminal domains; 4-chlorobenzoyl-CoA ligase (*62*) demonstrates values of 38.9 and 60.9 Å$^2$; and yeast acetyl-CoA synthetase (*63*) exhibits values of 34.4 and 69.0 Å$^2$. These structures were determined with resolutions between 2.0 and 2.3 Å. In recent structures of either a fungal NRPS adenylation domain (*64*) or firefly luciferase (*65*), the C-terminus is not sufficiently ordered to be included in the final model. Thus there is precedent for the conformational flexibility within the crystal structure of the C-terminal domains of members of this family.

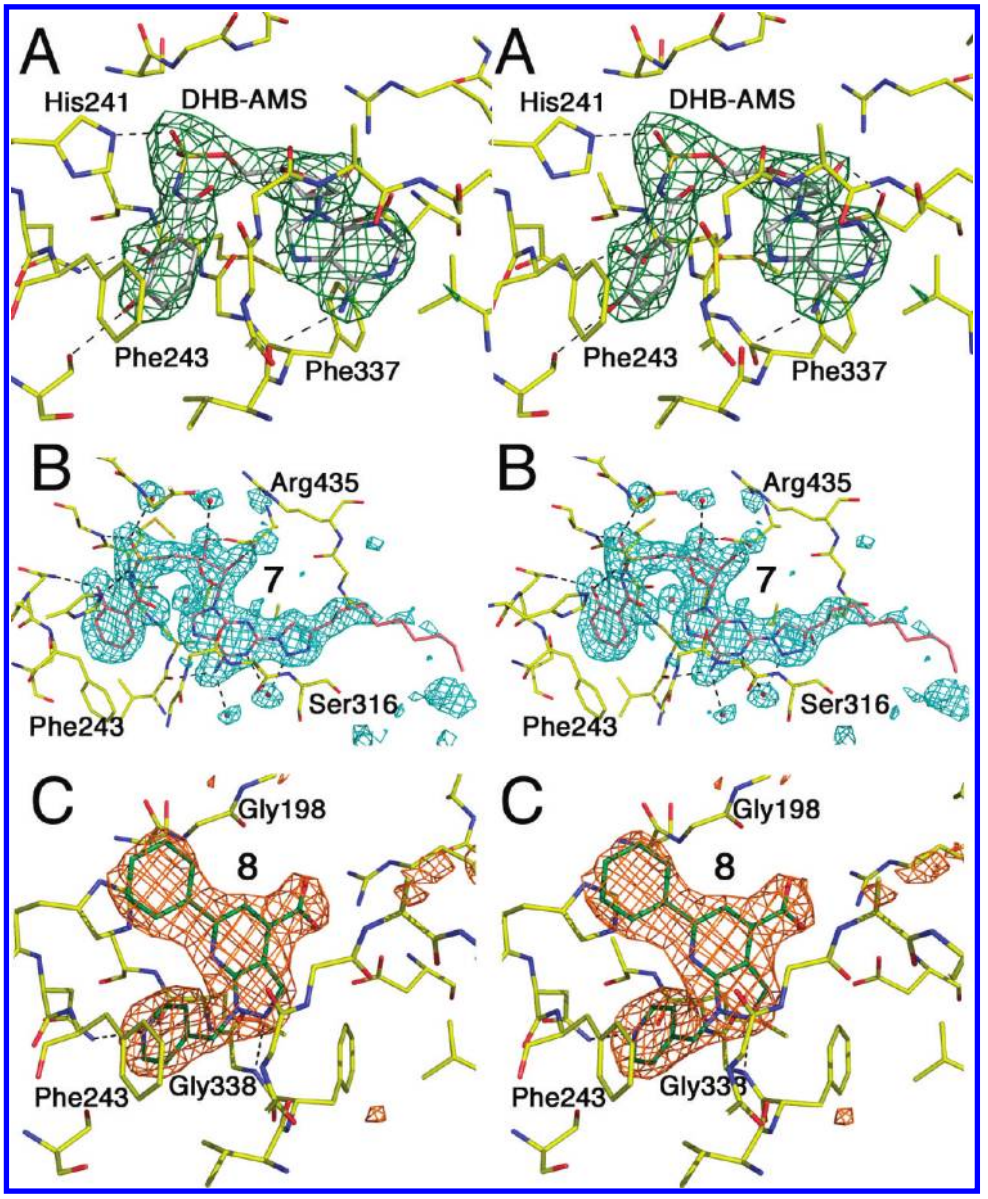


FIGURE 5: Electron density of BasE inhibitors. Electron density is shown in stereo representation for (A) **5**, (B) **7**, and (C) **8** bound to the BasE protein. The proteins are shown in approximately the same orientation as in Figure 4, and protein atoms are represented with yellow carbon atoms, blue nitrogen atoms, red oxygen atoms, and yellow sulfur atoms. The ligands are shown in their final refined positions and are colored the same except for carbon atoms, which are gray for **5**, pink for **7**, and green for **8**. Electron density maps, generated with coefficients of the form $F_o - F_c$ that were calculated prior to the inclusion of ligands in the molecular model, are shown contoured at $3\sigma$ in each panel. Several BasE protein residues are labeled. The aliphatic tail of **7** is weakly ordered. The density improved as refinement progressed, and 9 of the 12 carbon atoms are included in the final model for chain A.

The BasE structures bound to the inhibitors both contain two chains in the asymmetric unit. The final models for all three structures contain residues 3−437 for chain A and 3−438 for chain B. The two chains interact by forming an antiparallel continuous $\beta$-sheet with the final strand of the N-terminal domain. This strand is partially available to solvent in both of the catalytically relevant conformational states (*12*, *14*). The formation of this interaction in the crystal lattice prevents the C-terminal domain from adopting either of the catalytically relevant states, either of which would sterically interfere with the alternate chain. Pairwise structural alignments between BasE models bound to different ligands show that the rms distance for Cα positions is between 0.3 and 0.4 Å for all comparisons. There are no significant differences between the chains, and the discussion below will refer to chain A of the liganded complexes.

The BasE N-terminal domain is similar to the structure of prior members of the ANL superfamily of enzymes. The domain is composed of three $\beta$-sheets, terminating with the distorted $\beta$-sheet that leads to hinge residue at Lys437. A comparison to the N-terminal domain of DhbE show rms distance values of 1.0 Å for 387 structurally homologous residues. The most significant differences between BasE and the structure of DhbE occur at residues 135−185, a region of the N-terminal domain that is located ~20 Å from the active site. This region is the same in both chains of BasE and does not make contacts with symmetry-related molecules, suggesting this is a real difference between the structures BasE and DhbE. Given the location of this region, however, we do not believe this will impact the activity of the two proteins.

*Active Site Structures of BasE Bound to DHB-AMS* ***5***. The inhibitors bound very well to the BasE protein, and electron

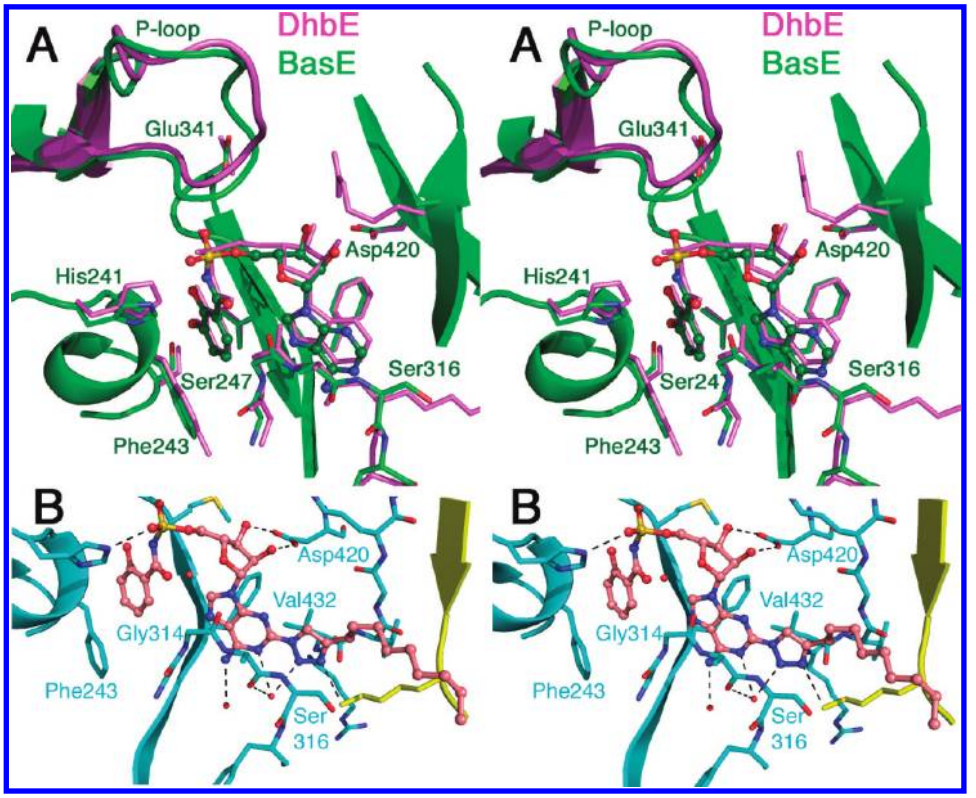


FIGURE 6: Ligand interactions for **5** and **7**. (A) Stereo figure of **5** superimposed with the structure of DhbE bound to the adenylate intermediate with DHB. DhbE is show in magenta, while BasE is shown in green. BasE residues are labeled. The side chains of homologous residues from DhbE are included. The ligand **5** is shown in ball-and-stick representation, while the DHB adenylate is shown with sticks only. (B) Stereo figure of **7** bound to BasE. Chain A, to which the ligand is bound, is shown in cyan. The ligand is shown in ball-and-stick representation with key interactions identified. Shown in yellow is the final $\beta$-strand of the alternate chain of BasE in the crystallographic asymmetric unit. The lysine side chain at position 437 interacts with the triazole ring of **7**.

density (Figure 5) unequivocally identifies the binding pocket. The DHB-AMS pocket is considered first as it is most similar to ligands present in other ANL superfamily members. The binding of DHB-AMS was compared to the binding of DHB-AMP to the DhbE protein (Figure 6A). There are no major differences between the active sites of the two enzymes in the residues that interact with the adenylate intermediate. The P-loop residues, Ser190−Lys198, adopt a different conformation, as has been observed previously (*13*, *15*, *60*, *62*, *66*). Given the role of these residues in binding the $\beta,\gamma$-phosphate moieties (*13*, *66*), it is not surprising that they are observed in different positions in the two structures. A second residue that adopts a different orientation between the two structures is Arg435, a completely conserved residue that has also been observed to play a role in binding the ribose hydroxyls of AMP by existing in multiple side chain orientations (*14*).

The bridging oxygen positioned between the phosphate and acyl or aryl substrate does not make specific interactions in any of the structures of members of this enzyme family. The nitrogen of the sulfamoyl mimic has a p$K_a$ of ~2 and is anticipated to be deprotonated. Tyr236 of DhbE is replaced by Phe243 of BasE that stacks similarly above the DHB ring. The two residues of DhbE that were identified by May et al. (*67*) as being used to discriminate between 2-hydroxybenzoyl- (salicyl-) and 2,3-dihydroxybenzoyl-adenylating domains, Ser240 and Val337, are indeed conserved as Ser247 and Val344 in BasE. The adenosyl sulfamate mimic has been used to crystallize firefly luciferase in the presence of the adenylate mimic as well and was shown to exhibit little effect on the binding of substrate in the active site (*68*).

*Binding of 7 to BasE*. Upon identification of the Sal-AMS **6** inhibitor of MbtA and other salicylate adenylating enzymes involved in siderophore synthesis (*33*, *34*, *37*), analysis of modeling data and structure−activity relationships (*39*, *69*) identified a pocket adjacent to the C2 position of the adenine base that might be exploited for improvement of the bisubstrate inhibitor. One such compound, **7** (Figure 1), has been identified that contains an *n*-dodecyltriazole moiety bound to the C2 position of the adenine ring (*41*). This compound exhibits an MIC of ~15 $\mu$M against *A. baumannii* in iron limiting condition and is inactive under iron replete conditions. Interestingly, the lipid tail is essential for activity since both DHB-AMS **5** and Sal-AMS **6** do not possess any antibacterial activity against *A. baumannii* (D. Wilson and C. Aldrich, unpublished results).

The structure of BasE bound to **7** was determined at 1.9 Å resolution. Electron density showed the binding position of the triazole ring and a portion of the aliphatic group (Figure 6B). Chain A contains nine methylene groups while chain B contains four. The additional binding affinity for the lipid tail is provided primarily by a pocket formed by the main chain of Gly314, Ala315, and Ser316 on one face and by Val432 and Val433 on the opposing face. Val433 initiates the final $\beta$-strand of the N-terminal domain, which then ends at Lys437, the hinge residue for the conformational change. As noted above, the strands from both chains in the crystal lattice form an antiparallel sheet. This positions the side chain of Lys437 from one chain near the triazole ring of the alternate active site (Figure 6B).

*Binding of **8** to BasE*. The structure of BasE bound to **8** was solved at 2.1 Å resolution. The electron density of the ligand allowed unequivocal placement of the compound in the model

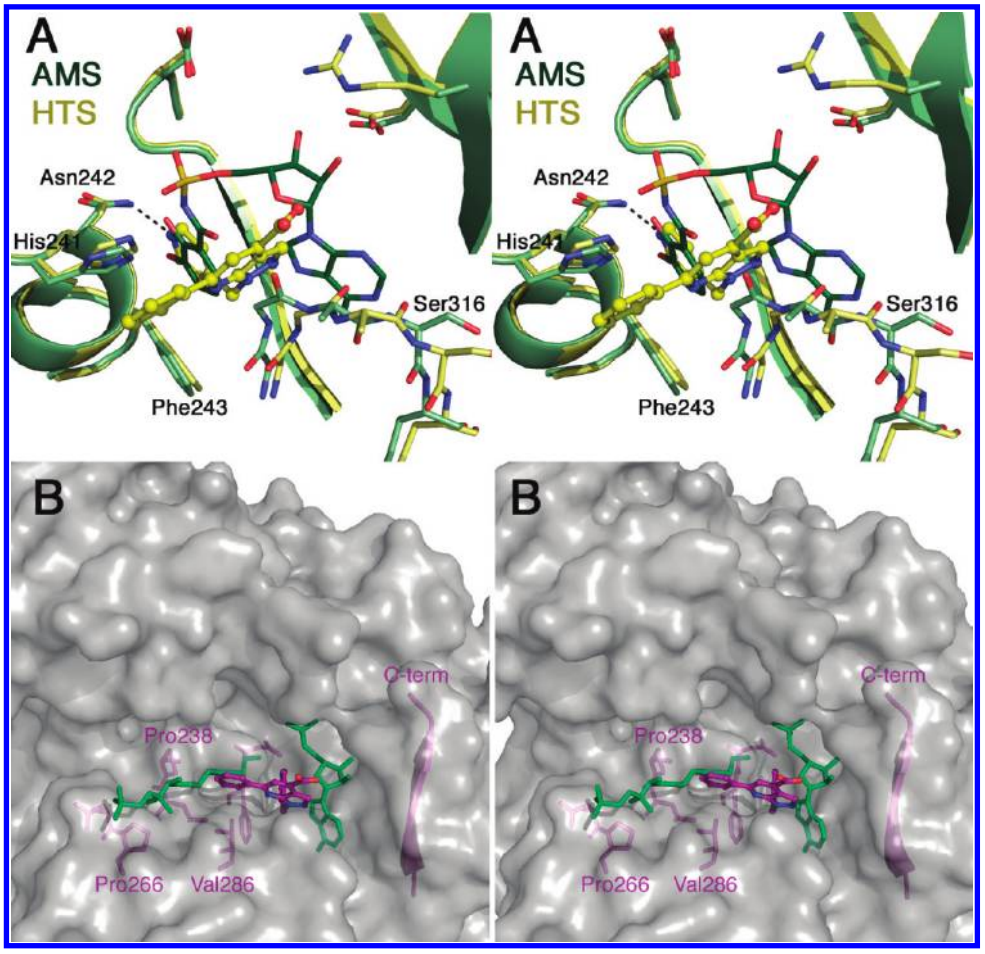


FIGURE 7: Interactions of inhibitor **8** with BasE. (A) Stereo figure of BasE bound to **8** superimposed with the structure of BasE bound to DHB-AMS **5**. BasE bound to **5** is shown in green, while the BasE structure bound to **8** is shown in yellow. The high-throughput inhibitor **8** is shown with ball-and-stick representation, while DHB-AMS **5** is shown with sticks. The 4-methylpyridyl group interacts with the side chain of Asn242. (B) Stereo representation of **8** bound to BasE. The BasE N-terminal domain is shown as a gray surface representation. Residues that abut the pantetheine binding pocket of related enzymes, Pro238, Phe243, Pro266, and Val286, are shown as purple sticks. The final strand of the N-terminal domain is included to orient the figure, and the position of the disordered C-terminal domain is noted. Superimposed in green are AMP and the pantetheine moiety from the related enzyme, 4-chlorobenzoyl-CoA ligase (PDB 3CW9). The figure illustrates the location of the phenyl ring of **8** in the pantetheine binding tunnel.

(Figure 5C). Prior structure−activity relationship studies with the salicyl-adenylating enzyme MbtA have identified that proximal to the adenine binding pocket was a second binding pocket that could accommodate an aromatic group. This extra binding pocket enabled the substituted nucleotide derivative 5′-*O*-[*N*-(2-hydroxybenzoyl)sulfamoyl]-2-phenyladenosine to bind to MbtA with a subnanomolar binding constant and suggested that the phenyl or pyridine ring of **8** may utilize this binding pocket (*39*).

Inhibitor **8** bound to BasE in an unexpected binding mode (Figure 7A). In the crystal complex, the 4-pyridylmethyl group occupies the DHB binding pocket. The ring nitrogen of the pyridine moiety accepts a hydrogen bond from the side chain of Asn242, in a manner that is similar to the 2- and 3-hydroxy groups of DHB in the DHB-AMS liganded structure. Additionally, the N2 nitrogen of the pyrazole ring of **8** forms a hydrogen bond with the amide nitrogen of Gly338 (Figure 5C). Illustrating binding of **8** in both the DHB and AMP subsites, the crystal structure corroborates the competitive inhibition pattern shown by **8** with respect to both substrates.

The hydrogen-bonding components of the aryl moiety of DHB-AMS are ortho and meta to the bridging carbonyl group that is connected to the sulfamoyladenosine moiety. In contrast, the pyridine nitrogen of **8** is para to the 4-methyl linker to the pyrazolo[3,4-*b*]pyridine. Because of these differences between the orientation of the hydrogen-bonding groups, the pyrazolo[3,4-*b*]pyridine moiety does not superimpose with the AMP of the adenylate binding pocket (Figure 7A). The new binding position of the pyrazolo moiety causes a reorientation of the loop containing Gly314-Ala315-Ser316. This loop has been observed to adopt different orientations in the homologous enzyme, 4-chlorobenzoyl-CoA ligase, where it fills the adenine pocket in the absence of ligand and stacks against the adenine ring in the presence of nucleotide (*62*).

The most unexpected feature of the binding of **8** to the BasE enzyme is that the phenyl ring, bound at the C2 position of the pyrazolo[3,4-*b*]pyridine scaffold, projects away from the adenylate binding pocket (Figure 7A). Indeed, superposition of the structure of 4-chlorobenzoyl-CoA ligase bound to the product analogue 4-chlorophenacyl-CoA and AMP (Figure 7B) demonstrates that the phenyl group of **8** projects into the pantetheine tunnel through which the pantetheine moiety of CoA or of the acyl-carrier protein approaches the active site. In this position, the phenyl group stacks against His241, a residue that is conserved as an aromatic residue in all ANL enzymes and exhibits a side chain rotation that reflects the conformational state of the protein (*12*). On the opposite side of the phenyl group,

the side chain of Val286 is present to provide hydrophobic contacts. Val286 is present in the N-terminal domain on a loop, Leu-Val-Pro, that is conserved in DhbE, YbtE, MbtA, VibE, and EntE.

We note also that residues from the disordered C-terminal domain may contribute interactions with the inhibitors. Given the quality of the electron density, the inhibitors in the crystal structure bind with high occupancy, and we believe that in all three cases the primary interaction energy is derived from the N-terminal domain. In the adenylate-forming conformation, the side chain of Lys526 likely interacts with the sulfamoyl group, as observed with other ANL superfamily members bound to adenylate or adenylate mimics. Additionally, the pantetheine tunnel that has been identified in members of the enzyme family that have been crystallized in the presence of CoA or CoA adducts is bordered by residues from both the N-terminal domain and the C-terminal residues that belong to the two-stranded $\beta$-sheet that follows the hinge residue. A universally conserved glycine residue on this loop, Gly439 in BasE, may also interact with the phenyl constituent of **8** if the enzyme were to adopt the thioester-forming conformation.

## CONCLUSIONS

The need to identify new targets that will enable the development of new strategies for antibiotic design has received a great deal of attention, both within the scientific and public literature. Directing compounds against the acquisition of important nutrients may provide novel routes. The fascinating biochemistry of the NRPS proteins and their involvement in siderophore biosynthesis has prompted these studies to functionally characterize BasE and structurally investigate the binding of inhibitors. The structure of the BasE adenylation domain described here illustrates the binding mode of three inhibitors, two that were designed based on the knowledge of the chemical mechanism (*33*, *34*, *41*) and a third that was identified through high-throughput screening efforts (*43*). The binding pocket of **8** identified through structural analysis identifies additional protein residues that could potentially interact with chemically modified secondary compounds. For example, the binding of the phenyl group within the pantetheine binding tunnel suggests that additional hydrophobic elements may further fill this tunnel, enabling tight binding.

Because of the vital need for iron for bacterial growth, some bacteria have evolved to produce multiple siderophores. Within *A. baumannii* ATCC strain 19606, interruption of the acinetobactin synthetase *basD* results in a clone that is unable to grow under iron-limiting conditions demonstrating the importance of acinetobactin (*70*). An alternate strain, ATCC17978, has been reported to contain a second genetic locus for siderophore biosynthesis such that a *basD* mutation is still able to grow in the presence of an iron chelator (*71*). Interestingly, this locus shares some similarity with the *V. cholerae* vibriobactin cluster and contains the genes necessary for the synthesis of DHB, suggesting that this siderophore likely also contains the aryl cap present in acinetobactin. This alternate cluster encodes a BasE homologue (Genbank accession ABO12991) that shares 35% sequence identity with the BasE protein of the acinetobactin cluster. All residues within 4 Å of the binding site of **8** are conserved between the two proteins, raising the possibility that the inhibitors designed against BasE may inhibit both siderophore synthetic pathways.

## ACKNOWLEDGMENT

We thank Dr. Anthony Campagnari (Department of Immunology and Microbiology, University at Buffalo) for the genomic DNA from the *A. baumannii* AB900 strain.

## REFERENCES

1. Clatworthy, A. E., Pierson, E., and Hung, D. T. (2007) Targeting virulence: a new paradigm for antimicrobial therapy. *Nat. Chem. Biol. 3*, 541–548.
2. Fischbach, M. A., and Walsh, C. T. (2009) Antibiotics for emerging pathogens. *Science 325*, 1089–1093.
3. Sandy, M., and Butler, A. (2009) Microbial iron acquisition: marine and terrestrial siderophores. *Chem. Rev. 109*, 4580–4595.
4. Neilands, J. B. (1981) Microbial iron compounds. *Annu. Rev. Biochem. 50*, 715–731.
5. Miethke, M., and Marahiel, M. A. (2007) Siderophore-based iron acquisition and pathogen control. *Microbiol. Mol. Biol. Rev. 71*, 413–451.
6. Lin, H., Fischbach, M. A., Liu, D. R., and Walsh, C. T. (2005) In vitro characterization of salmochelin and enterobactin trilactone hydrolases IroD, IroE, and Fes. *J. Am. Chem. Soc. 127*, 11075–11084.
7. Koglin, A., and Walsh, C. T. (2009) Structural insights into nonribosomal peptide enzymatic assembly lines. *Nat. Prod. Rep. 26*, 987–1000.
8. Weissman, K. J., and Muller, R. (2008) Protein-protein interactions in multienzyme megasynthetases. *ChemBioChem 9*, 826–848.
9. Lambalot, R. H., Gehring, A. M., Flugel, R. S., Zuber, P., LaCelle, M., Marahiel, M. A., Reid, R., Khosla, C., and Walsh, C. T. (1996) A new enzyme superfamily—the phosphopantetheinyl transferases. *Chem. Biol. 3*, 923–936.
10. Marahiel, M. A., and Essen, L. O. (2009) Chapter 13. Nonribosomal peptide synthetases mechanistic and structural aspects of essential domains. *Methods Enzymol. 458*, 337–351.
11. Tanovic, A., Samel, S. A., Essen, L.-O., and Marahiel, M. A. (2008) Crystal structure of the termination module of a nonribosomal peptide synthetase. *Science 321*, 659–663.
12. Gulick, A. M. (2009) Conformational dynamics in the acyl-CoA synthetases, adenylation domains of non-ribosomal peptide synthetases, and firefly luciferase. *ACS Chem. Biol. 4*, 811–827.
13. Kochan, G., Pilka, E. S., von Delft, F., Oppermann, U., and Yue, W. W. (2009) Structural snapshots for the conformation-dependent catalysis by human medium-chain acyl-coenzyme A synthetase ACSM2A. *J. Mol. Biol. 388*, 997–1008.
14. Reger, A. S., Wu, R., Dunaway-Mariano, D., and Gulick, A. M. (2008) Structural characterization of a 140° domain movement in the two-step reaction catalyzed by 4-chlorobenzoate:CoA ligase. *Biochemistry 47*, 8016–8025.
15. Gulick, A. M., Starai, V. J., Horswill, A. R., Homick, K. M., and Escalante-Semerena, J. C. (2003) The 1.75 Å crystal structure of acetyl-CoA synthetase bound to adenosine-5′-propylphosphate and coenzyme A. *Biochemistry 42*, 2866–2873.
16. Branchini, B. R., Southworth, T. L., Murtiashaw, M. H., Wilkinson, S. R., Khattak, N. F., Rosenberg, J. C., and Zimmer, M. (2005) Mutagenesis evidence that the partial reactions of firefly bioluminescence are catalyzed by different conformations of the luciferase C-terminal domain. *Biochemistry 44*, 1385–1393.
17. Drake, E. J., Nicolai, D. A., and Gulick, A. M. (2006) Structure of the EntB multidomain nonribosomal peptide synthetase and functional analysis of its interaction with the EntE adenylation domain. *Chem. Biol. 13*, 409–419.
18. Reger, A. S., Carney, J. M., and Gulick, A. M. (2007) Biochemical and crystallographic analysis of substrate binding and conformational changes in acetyl-CoA synthetase. *Biochemistry 46*, 6536–6546.
19. Wu, R., Cao, J., Lu, X., Reger, A. S., Gulick, A. M., and Dunaway-Mariano, D. (2008) Mechanism of 4-chlorobenzoate:coenzyme a ligase catalysis. *Biochemistry 47*, 8026–8039.
20. Wu, R., Reger, A. S., Lu, X., Gulick, A. M., and Dunaway-Mariano, D. (2009) The mechanism of domain alternation in the acyl-adenylate forming ligase superfamily member 4-chlorobenzoate: coenzyme A ligase. *Biochemistry 48*, 4115–4125.
21. Peleg, A. Y., Seifert, H., and Paterson, D. L. (2008) *Acinetobacter baumannii*: emergence of a successful pathogen. *Clin. Microbiol. Rev. 21*, 538–582.
22. Perez, F., Hujer, A. M., Hujer, K. M., Decker, B. K., Rather, P. N., and Bonomo, R. A. (2007) Global challenge of multidrug-resistant *Acinetobacter baumannii*. *Antimicrob. Agents Chemother. 51*, 3471–3484.

23. Calhoun, J. H., Murray, C. K., and Manring, M. M. (2008) Multidrug-resistant organisms in military wounds from Iraq and Afghanistan. *Clin. Orthop. Relat. Res. 466*, 1356–1362.
24. Yamamoto, S., Okujo, N., and Sakakibara, Y. (1994) Isolation and structure elucidation of acinetobactin, a novel siderophore from *Acinetobacter baumannii*. *Arch. Microbiol. 162*, 249–254.
25. Mihara, K., Tanabe, T., Yamakawa, Y., Funahashi, T., Nakao, H., Narimatsu, S., and Yamamoto, S. (2004) Identification and transcriptional organization of a gene cluster involved in biosynthesis and transport of acinetobactin, a siderophore produced by *Acinetobacter baumannii* ATCC 19606T. *Microbiology 150*, 2587–2597.
26. Sattely, E. S., and Walsh, C. T. (2008) A latent oxazoline electrophile for N-O-C bond formation in pseudomonine biosynthesis. *J. Am. Chem. Soc. 130*, 12282–12284.
27. Wuest, W. M., Sattely, E. S., and Walsh, C. T. (2009) Three siderophores from one bacterial enzymatic assembly line. *J. Am. Chem. Soc. 131*, 5056–5057.
28. Quadri, L. E. (2000) Assembly of aryl-capped siderophores by modular peptide synthetases and polyketide synthases. *Mol. Microbiol. 37*, 1–12.
29. Keating, T. A., Marshall, C. G., and Walsh, C. T. (2000) Reconstitution and characterization of the *Vibrio cholerae* vibriobactin synthetase from VibB, VibE, VibF, and VibH. *Biochemistry 39*, 15522–15530.
30. Raymond, K. N., Dertz, E. A., and Kim, S. S. (2003) Enterobactin: an archetype for microbial iron transport. *Proc. Natl. Acad. Sci. U.S.A. 100*, 3584–3588.
31. Krithika, R., Marathe, U., Saxena, P., Ansari, M. Z., Mohanty, D., and Gokhale, R. S. (2006) A genetic locus required for iron acquisition in *Mycobacterium tuberculosis*. *Proc. Natl. Acad. Sci. U.S.A. 103*, 2069–2074.
32. Quadri, L. E., Sello, J., Keating, T. A., Weinreb, P. H., and Walsh, C. T. (1998) Identification of a *Mycobacterium tuberculosis* gene cluster encoding the biosynthetic enzymes for assembly of the virulence-conferring siderophore mycobactin. *Chem. Biol. 5*, 631–645.
33. Ferreras, J. A., Ryu, J. S., Di Lello, F., Tan, D. S., and Quadri, L. E. (2005) Small-molecule inhibition of siderophore biosynthesis in *Mycobacterium tuberculosis* and *Yersinia pestis*. *Nat. Chem. Biol. 1*, 29–32.
34. Somu, R. V., Boshoff, H., Qiao, C., Bennett, E. M., Barry, C. E., III, and Aldrich, C. C. (2006) Rationally designed nucleoside antibiotics that inhibit siderophore biosynthesis of *Mycobacterium tuberculosis*. *J. Med. Chem. 49*, 31–34.
35. Miethke, M., Bisseret, P., Beckering, C. L., Vignard, D., Eustache, J., and Marahiel, M. A. (2006) Inhibition of aryl acid adenylation domains involved in bacterial siderophore synthesis. *FEBS J. 273*, 409–419.
36. Sikora, A. L., Wilson, D. J., Aldrich, C. C., and Blanchard, J. S. (2010) Kinetic and inhibition studies of dihydroxybenzoate-AMP ligase from *Escherichia coli*. *Biochemistry 49*, 3648–3657.
37. Qiao, C., Gupte, A., Boshoff, H. I., Wilson, D. J., Bennett, E. M., Somu, R. V., Barry, C. E., 3rd, and Aldrich, C. C. (2007) 5′-*O*-[(*N*-Acyl)sulfamoyl]adenosines as antitubercular agents that inhibit MbtA: an adenylation enzyme required for siderophore biosynthesis of the mycobactins. *J. Med. Chem. 50*, 6080–6094.
38. Vannada, J., Bennett, E. M., Wilson, D. J., Boshoff, H. I., Barry, C. E., III, and Aldrich, C. C. (2006) Design, synthesis, and biological evaluation of beta-ketosulfonamide adenylation inhibitors as potential antitubercular agents. *Org. Lett. 8*, 4707–4710.
39. Neres, J., Labello, N. P., Somu, R. V., Boshoff, H. I., Wilson, D. J., Vannada, J., Chen, L., Barry, C. E., III, Bennett, E. M., and Aldrich, C. C. (2008) Inhibition of siderophore biosynthesis in *Mycobacterium tuberculosis* with nucleoside bisubstrate analogues: structure-activity relationships of the nucleobase domain of 5′-*O*-[*N*-(salicyl)sulfamoyl]adenosine. *J. Med. Chem. 51*, 5349–5370.
40. Somu, R. V., Wilson, D. J., Bennett, E. M., Boshoff, H. I., Celia, L., Beck, B. J., Barry, C. E., III, and Aldrich, C. C. (2006) Antitubercular nucleosides that inhibit siderophore biosynthesis: SAR of the glycosyl domain. *J. Med. Chem. 49*, 7623–7635.
41. Gupte, A., Boshoff, H. I., Wilson, D. J., Neres, J., Labello, N. P., Somu, R. V., Xing, C., Barry, C. E., and Aldrich, C. C. (2008) Inhibition of siderophore biosynthesis by 2-triazole substituted analogues of 5′-*O*-[*N*-(salicyl)sulfamoyl]adenosine: antibacterial nucleosides effective against *Mycobacterium tuberculosis*. *J. Med. Chem. 51*, 7495–7507.
42. Cisar, J. S., Ferreras, J. A., Soni, R. K., Quadri, L. E., and Tan, D. S. (2007) Exploiting ligand conformation in selective inhibition of nonribosomal peptide synthetase amino acid adenylation with designed macrocyclic small molecules. *J. Am. Chem. Soc. 129*, 7752–7753.
43. Neres, J., Wilson, D. J., Celia, L., Beck, B. J., and Aldrich, C. C. (2008) Aryl acid adenylating enzymes involved in siderophore biosynthesis: fluorescence polarization assay, ligand specificity, and discovery of non-nucleoside inhibitors via high-throughput screening. *Biochemistry 47*, 11735–11749.
44. Kapust, R. B., Tozser, J., Fox, J. D., Anderson, D. E., Cherry, S., Copeland, T. D., and Waugh, D. S. (2001) Tobacco etch virus protease: mechanism of autolysis and rational design of stable mutants with wild-type catalytic proficiency. *Protein Eng. 14*, 993–1000.
45. Adams, M. D., Goglin, K., Molyneaux, N., Hujer, K. M., Lavender, H., Jamison, J. J., MacDonald, I. J., Martin, K. M., Russo, T., Campagnari, A. A., Hujer, A. M., Bonomo, R. A., and Gill, S. R. (2008) Comparative genome sequence analysis of multidrug-resistant *Acinetobacter baumannii*. *J. Bacteriol. 190*, 8053–8064.
46. Yin, J., Lin, A. J., Golan, D. E., and Walsh, C. T. (2006) Site-specific protein labeling by Sfp phosphopantetheinyl transferase. *Nat. Protoc. 1*, 280–285.
47. Jancarik, J., and Kim, S.-H. (1991) Sparse matrix sampling: a screening method for crystallization of proteins. *J. Appl. Crystallogr. 24*, 409–411.
48. Vagin, A., and Teplyakov, A. (1997) MOLREP: an automated program for molecular replacement. *J. Appl. Crystallogr. 30*, 1022–1025.
49. Stein, N. (2008) CHAINSAW: a program for mutating pdb files as templates for molecular replacment. *J. Appl. Crystallogr. 41*, 641–643.
50. McCoy, A. J., Grosse-Kunstleve, R. W., Adams, P. D., Winn, M. D., Storoni, L. C., and Read, R. J. (2007) Phaser crystallographic software. *J. Appl. Crystallogr. 40*, 658–674.
51. Murshudov, G. N., Vagin, A. A., and Dodson, E. J. (1997) Refinement of macromolecular structures by the maximum-likelihood method. *Acta Crystallogr., Sect. D: Biol. Crystallogr. 53*, 240–255.
52. McPhillips, T. M., McPhillips, S. E., Chiu, H. J., Cohen, A. E., Deacon, A. M., Ellis, P. J., Garman, E., Gonzalez, A., Sauter, N. K., Phizackerley, R. P., Soltis, S. M., and Kuhn, P. (2002) Blu-Ice and the distributed control system: software for data acquisition and instrument control at macromolecular crystallography beamlines. *J. Synchrotron Radiat. 9*, 401–406.
53. Emsley, P., and Cowtan, K. (2004) Coot: model-building tools for molecular graphics. *Acta Crystallogr., Sect. D: Biol. Crystallogr. 60*, 2126–2132.
54. May, J. J., Wendrich, T. M., and Marahiel, M. A. (2001) The *dhb* operon of *Bacillus subtilis* encodes the biosynthetic template for the catecholic siderophore 2,3-dihydroxybenzoate-glycine-threonine trimeric ester bacillibactin. *J. Biol. Chem. 276*, 7209–7217.
55. Rusnak, F., Faraci, W. S., and Walsh, C. T. (1989) Subcloning, expression, and purification of the enterobactin biosynthetic enzyme 2,3-dihydroxybenzoate-AMP ligase: demonstration of enzyme-bound (2,3-dihydroxybenzoyl)adenylate product. *Biochemistry 28*, 6827–6835.
56. Smith, M. G., Gianoulis, T. A., Pukatzki, S., Mekalanos, J. J., Ornston, L. N., Gerstein, M., and Snyder, M. (2007) New insights into *Acinetobacter baumannii* pathogenesis revealed by high-density pyrosequencing and transposon mutagenesis. *Genes Dev. 21*, 601–614.
57. Vallenet, D., Nordmann, P., Barbe, V., Poirel, L., Mangenot, S., Bataille, E., Dossat, C., Gas, S., Kreimeyer, A., Lenoble, P., Oztas, S., Poulain, J., Segurens, B., Robert, C., Abergel, C., Claverie, J. M., Raoult, D., Medigue, C., Weissenbach, J., and Cruveiller, S. (2008) Comparative analysis of acinetobacters: three genomes for three lifestyles. *PLoS One 3*, e1805.
58. Marahiel, M. A., Stachelhaus, T., and Mootz, H. D. (1997) Modular peptide synthetases involved in nonribosomal peptide synthesis. *Chem. Rev. 97*, 2651–2674.
59. Yu, M., Magalhaes, M. L., Cook, P. F., and Blanchard, J. S. (2006) Bisubstrate inhibition: theory and application to *N*-acetyltransferases. *Biochemistry 45*, 14788–14794.
60. Hisanaga, Y., Ago, H., Nakagawa, N., Hamada, K., Ida, K., Yamamoto, M., Hori, T., Arii, Y., Sugahara, M., Kuramitsu, S., Yokoyama, S., and Miyano, M. (2004) Structural basis of the substrate-specific two-step catalysis of long chain fatty acyl-CoA synthetase dimer. *J. Biol. Chem. 279*, 31717–31726.
61. Conti, E., Franks, N. P., and Brick, P. (1996) Crystal structure of firefly luciferase throws light on a superfamily of adenylate-forming enzymes. *Structure 4*, 287–298.
62. Gulick, A. M., Lu, X., and Dunaway-Mariano, D. (2004) Crystal structure of 4-chlorobenzoate:CoA ligase/synthetase in the unliganded and aryl substrate-bound states. *Biochemistry 43*, 8670–8679.
63. Jogl, G., and Tong, L. (2004) Crystal structure of yeast acetyl-coenzyme A synthetase in complex with AMP. *Biochemistry 43*, 1425–1431.

64. Lee, T. V., Johnson, L. J., Johnson, R. D., Koulman, A., Lane, G. A., Lott, J. S., and Arcus, V. L. (2010) Structure of a eukaryotic nonribosomal peptide synthetase adenylation domain that activates a large hydroxamate amino acid in siderophore biosynthesis. *J. Biol. Chem. 285*, 2415–2427.
65. Auld, D. S., Lovell, S., Thorne, N., Lea, W. A., Maloney, D. J., Shen, M., Rai, G., Battaile, K. P., Thomas, C. J., Simeonov, A., Hanzlik, R. P., and Inglese, J. (2010) Molecular basis for the high-affinity binding and stabilization of firefly luciferase by PTC124. *Proc. Natl. Acad. Sci. U.S.A. 107*, 4878–4883.
66. Osman, K. T., Du, L., He, Y., and Luo, Y. (2009) Crystal structure of *Bacillus cereus* D-alanyl carrier protein ligase (DltA) in complex with ATP. *J. Mol. Biol. 388*, 345–355.
67. May, J. J., Kessler, N., Marahiel, M. A., and Stubbs, M. T. (2002) Crystal structure of DhbE, an archetype for aryl acid activating domains of modular nonribosomal peptide synthetases. *Proc. Natl. Acad. Sci. U.S.A. 99*, 12120–12125.
68. Nakatsu, T., Ichiyama, S., Hiratake, J., Saldanha, A., Kobashi, N., Sakata, K., and Kato, H. (2006) Structural basis for the spectral difference in luciferase bioluminescence. *Nature 440*, 372–376.
69. Labello, N. P., Bennett, E. M., Ferguson, D. M., and Aldrich, C. C. (2008) Quantitative three dimensional structure linear interaction energy model of 5′-*O*-[*N*-(salicyl)sulfamoyl]adenosine and the aryl acid adenylating enzyme MbtA. *J. Med. Chem. 51*, 7154–7160.
70. Dorsey, C. W., Tomaras, A. P., Connerly, P. L., Tolmasky, M. E., Crosa, J. H., and Actis, L. A. (2004) The siderophore-mediated iron acquisition systems of *Acinetobacter baumannii* ATCC 19606 and *Vibrio anguillarum* 775 are structurally and functionally related. *Microbiology 150*, 3657–3667.
71. Zimbler, D. L., Penwell, W. F., Gaddy, J. A., Menke, S. M., Tomaras, A. P., Connerly, P. L., and Actis, L. A. (2009) Iron acquisition functions expressed by the human pathogen *Acinetobacter baumannii*. *Biometals 22*, 23–32.